Petroleum Science 20 (2023) 3638–3653

Contents lists available at ScienceDirect

Petroleum Science

journal homepage: www.keaipublishing.com/en/journals/petroleum-science

Original Paper

Erosion characteristics and simulation charts of sand fracturing casing perforation

Shan-Zhi Shi [a], Si-Song Zhang [b, **], Ning Cheng [a], Gang Tian [a], De-Zhi Zeng [b, *], Hui-Yong Yu [a], Xi Wang [b], Xin Zhang [b]

[a] Research Institute of Engineering Technology, PetroChina Xinjiang Oilfield Company, Karamay, 834000, Xinjiang, China
[b] State Key Laboratory of Oil & Gas Reservoir Geology and Exploitation, Southwest Petroleum University, Chengdu, 610500, Sichuan, China

ARTICLE INFO

Article history:
Received 25 September 2022
Received in revised form
16 February 2023
Accepted 1 June 2023
Available online 15 June 2023

Edited by Jia-Jia Fei

Keywords:
Sanding fracturing
Erosion
Numerical simulation
Casing perforation
Solid-liquid flow

ABSTRACT

Large-scale sand fracturing is a necessary means in the efficient exploitation of shale gas/oil. However, in the process of fracturing operation, the sand carrying fluid and proppant easily causes scouring and wear to production strings, especially the casing perforation system, which damage the wellbore integrity and deformation to affect the subsequent fracturing. For this problem, taking the actual construction conditions and perforation technology of an oilfield in western China as an example, the structural parameters of the downhole string were measured and the wall thickness reduction model of casing perforation suitable for large-displacement sand fracturing in horizontal well section was established. With software ANSYS-FLUENT, the casing perforation erosion under the conditions of different displacements, sand content and perforation sand-passing quantity in the process of sand fracturing was simulated and calculated. The influences of three parameters on perforation erosion and expansion were analyzed and the prediction chart of the influences of three main control factors on perforation erosion and expansion was established. The perforation erosion images after fracturing construction were obtained with the downhole eagle perforation logging technology. The logging chart results were compared with the downhole eagle perforation data. The error between the established numerical simulation calculation charts and the real logging data was about 5%, indicating that the simulation charts were the valuable reference.

1. Introduction

Unconventional oil and gas play an important role in global energy consumption (Hossain et al., 2018; Melikoglu, 2014; Chen et al., 2020). China is rich in shale oil/gas resources, with low proven rate and huge potential (Yang et al., 2021). Accelerating the development of shale oil/gas has an important strategic role and practical significance in increasing clean energy supply, optimizing and adjusting the energy structure, alleviating the contradiction between energy supply and demand, and ensuring national energy security (Zheng et al., 2022). Based on the geological characteristics of shale reservoir, in order to achieve cost-effective development of shale oil/gas, the breakthrough and large-scale popularization of horizontal well technology and staged hydraulic fracturing technology are necessary technical means (Zeng et al., 2022).

However, with the finalization of the main process parameters and the development of most oil and gas wells entering the middle and late stages, and under the dual pressure of international oil prices and production increase effects, cost reduction and efficiency increase are imminent (Mohammed et al., 2020). The promotion and application of new fracturing technology of intensive stage + high-intensity proppant injection for shale gas reservoirs have improved the fracturing construction efficiency and reduced the single well fracturing cost, but also increased the risk of casing string deformation and damage (Zhao et al., 2020). At present, the deformation and damage of production layer casing after large-scale fracturing has become one of the bottleneck technical problems restricting the safe and efficient development of shale oil/gas (Bakhshi et al., 2021; Al-Fatlawi et al., 2019).

* Corresponding author.
** Corresponding author.
E-mail addresses: zhangsisong1995@163.com (S.-S. Zhang), zengdezhiswpu@163.com (D.-Z. Zeng).

https://doi.org/10.1016/j.petsci.2023.06.001

Roberts et al. (2020) directly observed and recorded the shape and size of perforations before and after fracturing by using downhole photography devices. Video comparison shows that proppant will abrade perforations during hydraulic fracturing (Fig. 1). The signs of casing perforation erosion have been clearly found through gravel flowback during fracturing production on the site. The maximum diameter of gravel can reach 30 mm, while the diameter of perforations is about 10 mm. When the casing perforation erosion occurs, the strength performance of the string will be reduced, which will lead to deformation failure and other accidents.

Erosion has been widely concerned in the early 20th century. The erosion of casing and perforation during sand fracturing belongs to the solid-liquid erosion and many factors affect the corrosion resistance of materials. Since the last century, relevant scholars have conducted theoretical research on the erosion problems and put forward various theories on material erosion (Table 1). Due to the development of modern computer science, numerical simulation, finite element analysis, and other disciplines, CFD (Computational Fluid Dynamics) numerical simulation method of computational fluid dynamics has been widely used in the research of erosion problems in oil and gas fields. Table 2 shows the studies on string and perforation erosion at home and abroad.

In recent years, computational fluid dynamics (CFD) or experimental methods have been used to study the particle erosion behaviors in the flow field, many factors affecting the particle erosion behaviors, and some optimization suggestions have been proposed (Table 2). The erosion of casing perforation system effect brought by sand fracturing will mainly lead to expansion of perforation, the thinning of wall thickness and affect the integrity of the wellbore, as well as change the friction and pressure drop from the wellbore to the formation, reduce its flow limiting effect and ultimately lead to the non-uniform extension of the fracture, which will affect the fracturing effect. However, at present, the research objects on solid-liquid phase erosion are mostly focused on surface pipelines and equipment, while the research on casing perforation erosion is rarely reported. The impact of large-scale sand fracturing induced erosion is still unclear, which needs urgent attention.

The study aims to explore the perforation erosion in the process of sand fracturing. The corresponding mathematical model was established. Based on the working conditions and perforation technology on site, the structural parameters of downhole casing were measured and the flow model and erosion model of large-displacement sand fracturing casings for horizontal well sections established. With the CFD software ANSYS-FLUENT, the effects of fracturing displacement, the sand content of fracturing fluid, and sand-passing quantity on the erosion characteristics of casing perforation and its vicinity were studied. The perforation erosion charts under different working conditions are established, which can estimate the casing perforation expansion value according to different construction conditions, optimize the perforation process parameters and maintain the balanced development of each fracture in combination with the specific needs of perforation flow limiting, so as to provide the technical basis for on-site fracturing reconstruction.

2. Model establishment and solution method

2.1. Geometric model and mesh

The research objects are the casing (TP125V, φ = 127 mm) commonly used in sand fracturing operation field in the west of China. The parameters of the casing are provided as: wall thickness = 11.1 mm, and inner diameter = 108 mm. The 3D modeling tool is used to establish the geometric model of the single perforation casing while retaining the perforation and the adjacent pipe section structure. The modeling results are shown in Fig. 2(a). The drainage basin in the pipe of the geometric model is extracted and the perforated casing basin model is constructed, as shown in Fig. 2(b). The original diameter of perforating is 10 mm regular round perforation.

Using the MESH block in the ANSYS Workbench software, the unstructured tetrahedral mesh is used to mesh the three-dimensional model of the basin, and the wall, perforation are locally densified. The boundary layers present near the perforation and casing wall with five-layer grids (the cell height of the first layer is 0.4 mm, the growth factor is 1.3 and the y + value is 50), to enhance the reliability of the calculation results. In order to reduce the dispersion error caused by the number of grids, six groups of grids with different numbers are used for calculation, as shown in Fig. 3. When the number of grids exceeds 450,000, the calculation results tend to be stable.

Considering the calculation accuracy and solution resources, this paper finally selects the fifth set of grids with a number of 450,000 or so for subsequent calculation. The basin model grid in the perforated casing and the local grid of the pipe wall basin near the perforation are shown in Fig. 4.

2.2. Model of fluid flow and particle trajectory

This paper mainly focuses on the liquid-solid two-phase flow of sand carrying fluid and proppant in perforated casing during sand fracturing. The liquid phase, as a continuous phase, carries solid particles at high speed (Costa et al., 2018; Wang, 2020). The continuity and momentum equation can be expressed as:

$$\frac{\partial \rho}{\partial t} + \nabla(\rho u) = 0 \tag{1}$$

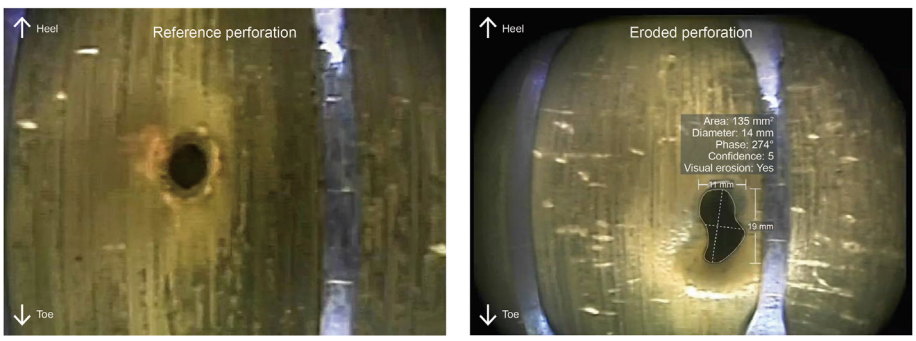

Fig. 1. Eagle logging images of perforation erosion and expansion (Roberts et al., 2020).

Table 1
Classical erosion theories.

References	Erosion theories	Materials to be explored	Results and conclusions
Finnie and McFadden (1958, 1978)	Micro cutting theory	Ductile material	The relationship between erosion rate, erosion angle, and erosion speed could be described quantitatively.
Bitter (1963)	Deformation and cutting wear theory	Plastic material	It was proposed that erosion wear consisted of impact load and cutting action.
Tilly (1973, 1979)	Two stage erosion theory	Ductile material	The erosion problem of brittle particles with large incident angle was well explained.
Fleming and Suh (1977)	Wear delamination theory	Plastic material	The main erosion angle range of particle erosion target was proved.
Evans (1978)	Elastic plastic indentation fracture theory	Brittle materials	The effects of sand and wall properties on erosion wear were explained.
Hutchings (1981)	Low cycle fatigue theory	Aluminum alloy material	The relationship between funnel volume, erosion rate and erosion angle of target plate after erosion was predicted.
Levy (1983)	Forging extrusion theory	Ductile material	The surface of the target was deformed and broken by the impact of particles.

Table 2
Studies on erosion of pipe string and perforation.

References	Targets to be explored	Results and conclusions
Parsi et al. (2015a, b)	Vertical pipes	The effects of apparent gas-liquid velocity, particle size, and liquid viscosity on the erosion rate and the location of serious erosion were given.
Suzuki et al. (2008)	90-degree bend	The effects of solid particle trajectory and near-wall function on erosion were studied.
Jignesh and Jyotirmay (2016)	Horizontal pipe	The effects of three main subtypes of intermittent flow on erosion were studied. Based on the theory of interface dynamics, four main erosion mechanisms in the pipeline were predicted.
Xu et al. (2021)	Buckling tubing	The erosion process of flowing sand on buckling tubing strings was studied from the aspects of buckling fluid channel, sand production parameters, fluid density, pressure, and end viscosity of buckling tubing strings.
Zhu et al. (2012)	Drill pipe	The flow erosion of drill pipe during gas drilling was studied by CFD method and the influences of drill pipe structure on erosion and the optimization scheme to reduce the slope of drill pipe joint were put forward.
Zhang et al. (2016)	High-pressure pipes	In the process of hydraulic fracturing, the failure reason and mechanism of high-pressure elbow were obtained through failure analysis, and the test results were verified by test and CFD method.
Zeng et al. (2018)	Elbow	Based on the consideration of the interaction between particles and wall in the gas-solid two-phase flow, the effects of flow pattern, particle sphericity, and motion trajectory on the erosion trace of casing wall were studied.
Long et al. (2017, 2018)	Perforation-erosion model	The geometric changes of perforations and their effects on bottom perforation pressure, fluid distribution and fracture extension were studied.
Crump and Conway (1988)	Perforated casing	The effects of different concentrations of mortar pumped into porous casing at different speeds were studied and the changes of erosion degree and pressure coefficient were studied.

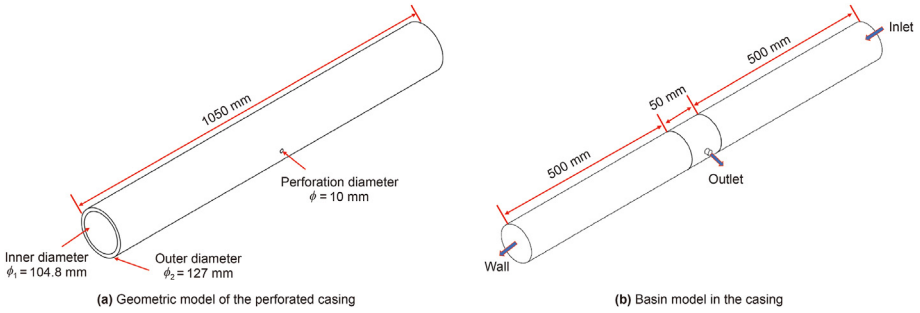

Fig. 2. Perforation casing erosion model.

$$\frac{\partial}{\partial t}(\rho u)+\nabla\cdot(\rho u u)=-\nabla P+\nabla\cdot\tau+\rho_g+S_M \tag{2}$$

where ρ is the density of the liquid continuous phase, kg/m^3; u is the velocity of continuous phase liquid, m/s. P is pressure, Pa; τ is the viscous stress applied on the fluid micro-element, N; ρ_g is the gravity of the liquid continuous phase, N; S_M is the momentum increment of the liquid continuous phase caused by small solid particles in the discrete phase, kg·m/s.

In this study, the high-speed fluid medium carrying solid particles belongs to a turbulent flow. Launder and Spalding (1974) proposed the standard k-ε model. In the standard k-ε model, the turbulent kinetic energy equation k and dissipation rate ε can be expressed as:

$$\frac{\partial(\rho_{mx}k)}{\partial t}+\frac{\partial(\rho_{mx}ku_i)}{\partial x_i}=\frac{\partial}{\partial x_j}\left[\left(\mu_{mx}+\frac{\mu_t}{\sigma_k}\right)\frac{\partial k}{\partial x_j}\right]+G_k+G_b-\rho_{mx}\varepsilon-Y_M \tag{3}$$

$$\frac{\partial(\rho_{mx}\varepsilon)}{\partial t}+\frac{\partial(\rho_{mx}\varepsilon u_i)}{\partial x_i}=\frac{\partial}{\partial x_j}\left[\left(\mu_{mx}+\frac{\mu_t}{\sigma_\varepsilon}\right)\frac{\partial \varepsilon}{\partial x_j}\right]+\rho_{mx}C_1E\varepsilon-\rho C_2\frac{\varepsilon^2}{k+\sqrt{v\varepsilon}}+C_{1\varepsilon}\frac{\varepsilon}{k}C_{3\varepsilon}G_b \tag{4}$$

where C_2, C_3 are constant,

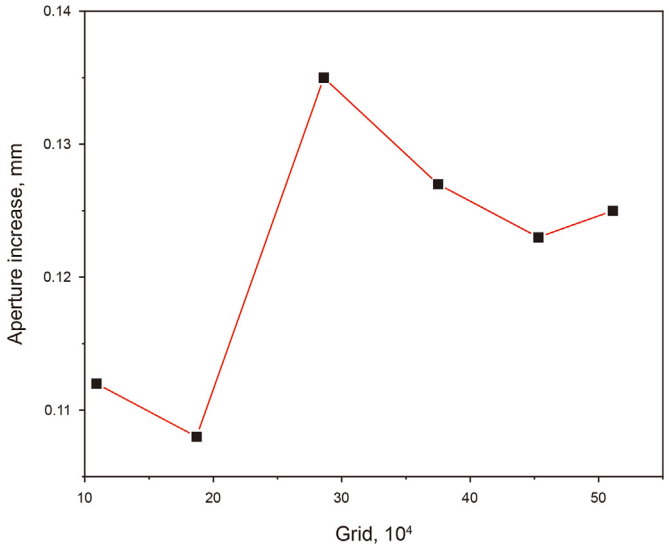

Fig. 3. Mesh grid-independence analysis.

$$\mu_t = \rho C_2 \frac{\varepsilon^2}{k} \tag{5}$$

$$C_1 = \max\left(0.43, \frac{\eta}{\eta + 5}\right) \tag{6}$$

$$\eta = (2E_{ij} \cdot E_{ij})^{\frac{1}{2}} \frac{k}{\varepsilon} \tag{7}$$

$$E_{ij} = \frac{1}{2}\left(\frac{\partial u_i}{\partial x_j} + \frac{\partial u_j}{\partial x_i}\right). \tag{8}$$

During sand fracturing, the sand content can exceed 20% and it is prone to lead to particle aggregation at the perforation. The dense discrete phase model (DDPM) is used to overcome the limitations of discrete phase volume fraction and Euler model is selected as the multiphase flow model.

2.3. Erosion wall thickness thinning model

The impact velocity and impact angle of each particle on the wall are predicted according to the CFD model, and then the erosion rate is calculated according to the erosion model. On the basis of erosion rate, the erosion time and target material properties are introduced to calculate the wall thickness thinning of casing in a certain erosion time. Wall thickness thinning can be expressed as (Zhang et al., 2007; ANSYS Inc, 2020; Zhang, 2006):

$$E_L = \sum_1^N \frac{\dot{m}_p C(d_p) f(\alpha) v_p^{b(v_p)}}{A_{face}} \cdot \frac{1.559 \times 10^{-3} B^{-0.59} F_s t}{\rho_L} \tag{9}$$

$$f(\alpha) = \begin{cases} 2.27\alpha^2 - 3.84\alpha^2, \alpha \le 15.3 \\ 3.147 \cos^2 \alpha \sin \alpha + 0.36 \sin^2 \alpha + 2.53, \alpha > 15.3 \end{cases} \tag{10}$$

where E_L is wall thickness thinning, mm; $\dot{m}_p$ is mass flow, kg/s; $C(d_p)$ is the function of proppant particle diameter; α is the impact angle of proppant particles on the wall, rad; $f(\alpha)$ is the function of impact angle; v_p is the velocity of proppant particles relative to the inner wall of casing, m/s; $b(v_p)$ is the function of the relative velocity of proppant particle, and A_{face} is the area of the cell face at the wall, ρ_L is the density of TP125V casing pipe, kg/m^3; F_s is the shape factor of proppant particles; t is erosion time, B is the Brinell hardness factor of the eroded surface material.

Perforation diameter expansion and casing wall thickness loss are interpreted as follows. The inner wall of casing is constantly collided by proppant particles, thus gradually resulting in the abrasion of wall material and the continuous reduction of final mass (Fig. 5). According to the field data and some experimental data, the erosion or diameter expansion of perforation is not a uniform process and the perforation gradually becomes a “horn” opening. With the increase in casing wall thickness loss near the perforation, the “horn” opening gradually becomes large, so the wall thickness loss near the perforation can be converted into the average diameter expansion of perforation as follows:

$$d_L = \sqrt{\frac{E_L A_s}{2\pi H}} - R, \tag{11}$$

where d_L is the average diameter expansion of the perforation, mm; H is the thickness of casing wall, mm; R is the initial perforation radius, mm; E_L is wall thickness loss, mm; A_s is erosion area, mm^2.

2.4. Boundary conditions and solution methods

As shown in Fig. 2(b). The inlet of perforated casing section is the velocity inlet boundary condition affected by single perforation displacement. The fracturing operation was a single-stage and multi-perforation fracturing process. The fracturing scheme in stage in the study was 6 clusters in a single stage with 3 perforations in each cluster. The displacement range of a single perforation was calculated with the total construction displacement and the number of clusters in a single stage on site, calculated displacement was converted into liquid phase velocity. The outlet pressure

Fig. 4. Basin model in perforated casing and local grids of the casing wall basin near the perforation.

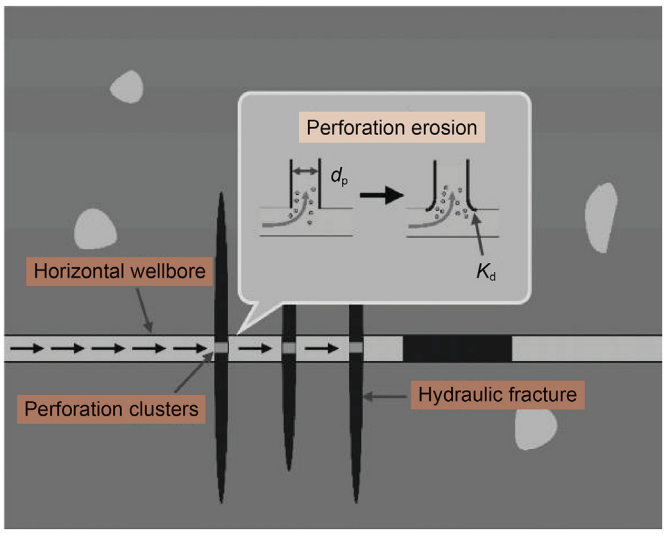

Fig. 5. Schematic diagram of perforation erosion.

boundary is located at the outlet cross section of the perforation to simulate the ambient static pressure environment. Particles are injected from the inlet of the fluid domain in the form of passing surfaces.

Based on the solver of pressure, this paper uses a SIMPLE algorithm to solve. The unit fluid medium is incompressible polymer slickwater, thermal effect of the fluid can not be ignored, temperatures at the inlet of the casing and the outlet of the perforation are constant, and solid particles are spherical particles. Second-order upwind scheme is employed to solve the momentum equation. The residual convergence criterion is set as 10^{-5} (Pereira et al., 2014; Parsi et al., 2015a, b).

Based on the erosion behaviors of proppant particles in the fracturing fluid on the perforation during sand fracturing, three main fracturing parameters affecting the erosion of casing perforation were obtained as: displacement, sand content (volume concentration) of fracturing fluid and sand-passing quantity of perforation. The simulation conditions are as follows: the single perforation fracturing displacement of 0.28–0.83 m^3/min (total displacement of single stage is 5~15 m^3/min), the sand content of 8%–23%. The proppant particles are quartz sand commonly used in oilfield fracturing construction, the particle size is 40/70 mesh, the bulk density is 1500 kg/m^3, and the sand-passing quantity of perforation is 0.67–5.67 m^3 (1000–8500 kg). The simulated conditions were set according to the actual working conditions of a well in an oil field in the western China. The working conditions are shown in Table 3.

3. Influences of sand fracturing parameters on casing perforation erosion

3.1. Influences of displacement on perforation erosion

The erosion of casing and perforations is caused by the collision between high-speed proppant particles and casing wall (Wu et al., 2022). Fracturing fluid carries proppant particles and exerts force on particles, so that particles collide with casing wall, constantly abrade casing wall, and continuously reduce casing mass, thus directly leading to the erosion and expansion of perforations and the thinning of casing wall thickness.

Under the quantity of sand-passing through the perforation (0.67 m^3), the sand content (11%), and six working conditions of single perforation fracturing displacement (0.28, 0.39, 0.5, 0.61, 0.72, and 0.83 m^3/min), the erosion degree of perforation and casing wall was simulated and calculated. In the cloud diagrams of casing wall thickness near the perforation after erosion under different fracturing displacements (Fig. 6), with the continuous increase in displacement, the wall thickness near the perforation in the flow inlet direction gradually became thin and the wall thickness thinning diffusion area also gradually increased and extended from the initial small piece to the two wings. A rabbit ear-shaped thinning trend was formed under the two working conditions of 0.72 and 0.83 m^3/min.

The average wall thickness loss of the casing wall near the perforation was converted into the average diameter expansion of the perforation with Eq. (11). With the continuous increase in fracturing displacement, the perforation diameter increased (Fig. 7). When the displacement increased from 0.28 to 0.83 m^3/min, the perforation diameter increased from 0.088 to 0.33 mm. The fitting function indicated that the slope of the diameter expansion curve increased with the increase in displacement.

3.2. Influences of sand content on perforation erosion

When the quantity of sand-passing through the perforation was 0.67 m^3 and the single perforation fracturing displacement was 0.5 m^3/min, the erosion degrees of perforation and casing wall under six sand content of fracturing fluid (8%, 11%, 14%, 17%, 20%, and 23%) were simulated and calculated. In the cloud diagrams of casing wall thickness near the perforation after erosion under different sand content of fracturing fluid (Fig. 8), with the continuous increase in sand content, the wall thickness near the perforation in the flow inlet direction gradually became thin and the wall thickness thinning diffusion area also gradually increased and extended from a small piece at the beginning to both wings so as to form a rabbit ear-shaped thinning trend. In the simulation results under different displacement conditions, the wall thickness loss and diffusion area increased significantly with the increase in sand content. When the sand content was 23%, the wall thickness near the perforation was close to 0 and the erosion was more serious.

The average wall thickness loss of the casing wall near the perforation was converted into the average diameter expansion of the perforation with Eq. (11). The perforation diameter expansion increased with the continuous increase in the sand content in fracturing fluid (Fig. 9). When the sand content increased from 8% to 23%, the perforation diameter expansion increased from 0.073 to 0.48 mm. In the fitting results, the slope of the diameter expansion curve increased with the increase in sand content.

3.3. Influences of sand-passing quantity on perforation erosion

When the single perforation fracturing displacement was 0.5 m^3/min and the sand content of fracturing fluid was 20%, the erosion degrees of perforation and casing wall under six sand-passing quantities (0.67, 1.67, 2.67, 3.67, 4.67 and 5.67 m^3) were simulated and calculated. In the wall thickness cloud diagrams of the casing near the perforation after erosion under different sand-passing quantities (Fig. 10), with the continuous increase in the sand-passing quantity, the casing wall thickness near the perforation in the flow inlet direction gradually became thin and the wall

Table 3
Simulation conditions of perforation and casing wall erosion wall thickness loss.

Sand-passing quantity of perforation, m^3	Displacements, m^3/min	Sand content, %
0.67	0.61	8, 11, 14, 17, 20, and 23
1.67	0.61	8, 11, 14, 17, 20, and 23
2.67	0.61	8, 11, 14, 17, 20, and 23
3.67	0.61	8, 11, 14, 17, 20, and 23
4.67	0.61	8, 11, 14, 17, 20, and 23
5.67	0.61	8, 11, 14, 17, 20, and 23
0.67	0.28, 0.39, 0.5, 0.61, 0.72 and 0.83	20
1.67	0.28, 0.39, 0.5, 0.61, 0.72 and 0.83	20
2.67	0.28, 0.39, 0.5, 0.61, 0.72 and 0.83	20
3.67	0.28, 0.39, 0.5, 0.61, 0.72 and 0.83	20
4.67	0.28, 0.39, 0.5, 0.61, 0.72 and 0.83	20
5.67	0.28, 0.39, 0.5, 0.61, 0.72 and 0.83	20
0.67	0.28	8, 11, 14, 17, 20, and 23
0.67	0.39	8, 11, 14, 17, 20, and 23
0.67	0.5	8, 11, 14, 17, 20, and 23
0.67	0.61	8, 11, 14, 17, 20, and 23
0.67	0.72	8, 11, 14, 17, 20, and 23
0.67	0.83	8, 11, 14, 17, 20, and 23

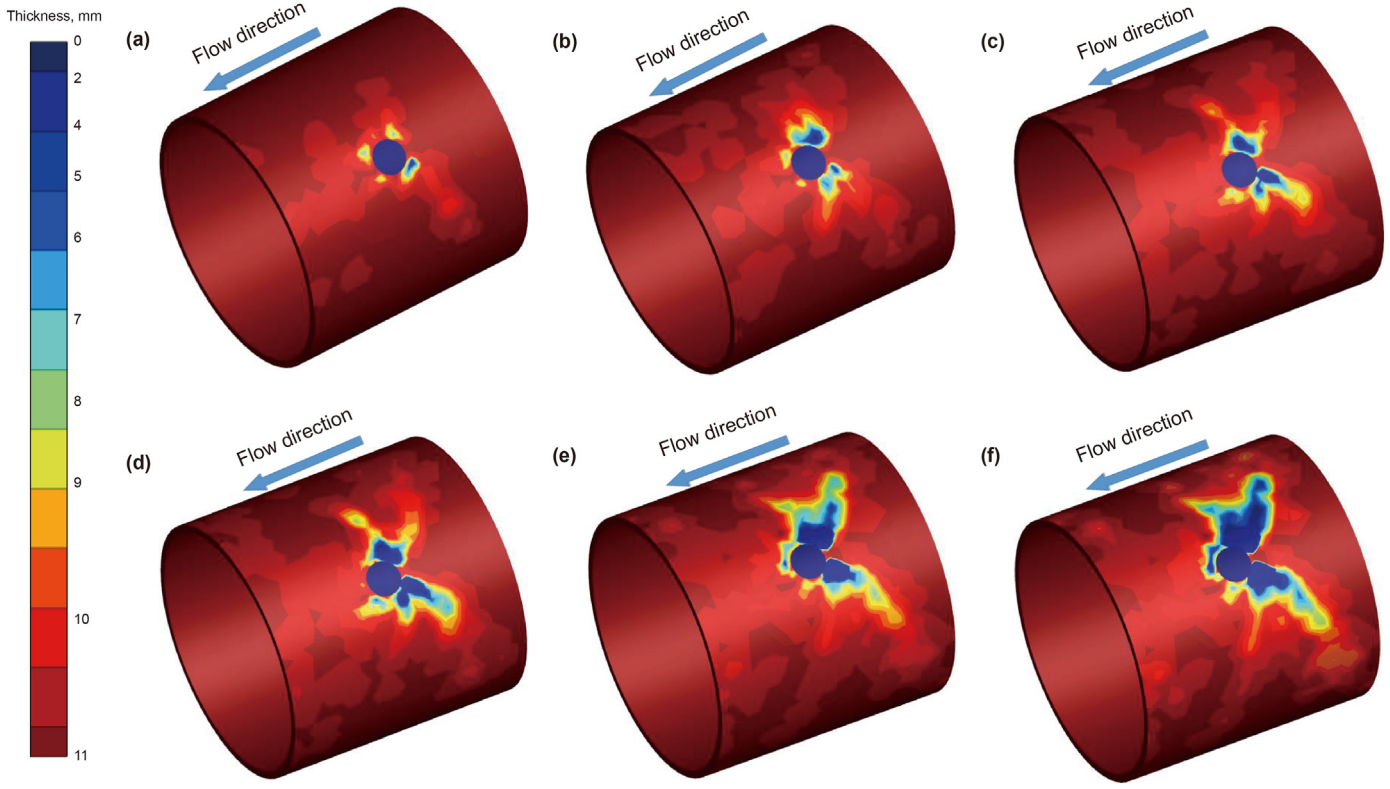

Fig. 6. Cloud diagrams of casing wall thickness near the perforation after erosion under different displacement conditions: (**a**) 0.28 m^3/min, (**b**) 0.39 m^3/min, (**c**) 0.5 m^3/min, (**d**) 0.61 m^3/min, (**e**) 0.72 m^3/min, and (**f**) 0.83 m^3/min.

thickness thinning diffusion area also gradually increased. In the cloud diagrams obtained under different sand-passing quantities and different sand content, the rabbit ear-shaped thinning trend with the increase in sand-passing quantities was also formed.

Compared with the cloud diagrams obtained under different sand content (Fig. 8), the cloud diagrams obtained under different sand-passing quantities (Fig. 10) showed the more obvious increase in wall thickness loss and diffusion area. When the sand-passing quantity reached 3.67 m^3, the wall thickness loss occurred at the back of the perforation. When the sand-passing quantity of the perforation reached 5.67 m^3, the casing wall at the back of the perforation was seriously eroded and the wall thickness of the casing wall near the perforation was close to 0, thus resulting in serious erosion.

The average wall thickness loss of the casing near the perforation was converted into the average diameter expansion of the perforation with Eq. (11). The perforation diameter expansion increased with the continuous increase of the sand-passing

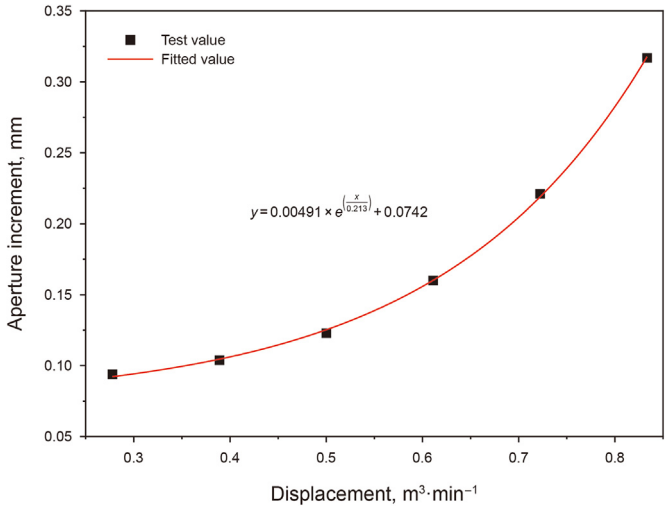

Fig. 7. Perforation diameter expansion after erosion under different displacement conditions.

quantity of the perforation (Fig. 11). When the sand-passing quantity of the perforation increased from 0.67 to 5.67 m^3, the perforation diameter expansion increased from 0.33 to 2.23 mm. In the fitting results, the slope of the expanding volume curve decreased with the increase in sand-passing quantity, the edge angle of the interface between the initial perforation and the inner wall of the casing was prominent and the surface was rough. Proppant particles and fluids had a strong impact on the material surface. However, after erosion, the material surface gradually became smooth and the mass loss of the metal material caused by the same sand-passing quantity was reduced, the average erosion rate was reduced accordingly. The wall material at the perforation was constantly lost, and the perforation diameter gradually became larger, thus decreasing the flow velocity at the casing perforation under the same displacement. The flow velocity was an important factor affecting the erosion rate. The reduced flow velocity inevitably decreased the average erosion rate at the perforation and thus the perforation expansion rate. It was inferred that due to the continuous erosion, the perforation expansion would reach a critical value.

3.4. Analysis of the main controlling factors of perforation erosion

The influences of fracturing construction parameters can be analyzed through exploring the correlation between these parameters and perforation erosion. If a parameter has the more significant influence, the correlation between this parameter and perforation erosion is more significant. The grey correlation analysis (GCA) method based on grey process can determine the benchmark sequence and several sub-sequences to obtain a weighted matrix and then the data are quantified with a specific statistical model to obtain the correlation between each factor and the actual result (Zhu et al., 2019; Shi et al., 2019). With the results calculated with the model and the actual construction working conditions in the site, the initial sequences for the grey correlation analysis of erosion impact were constructed (Table 4).

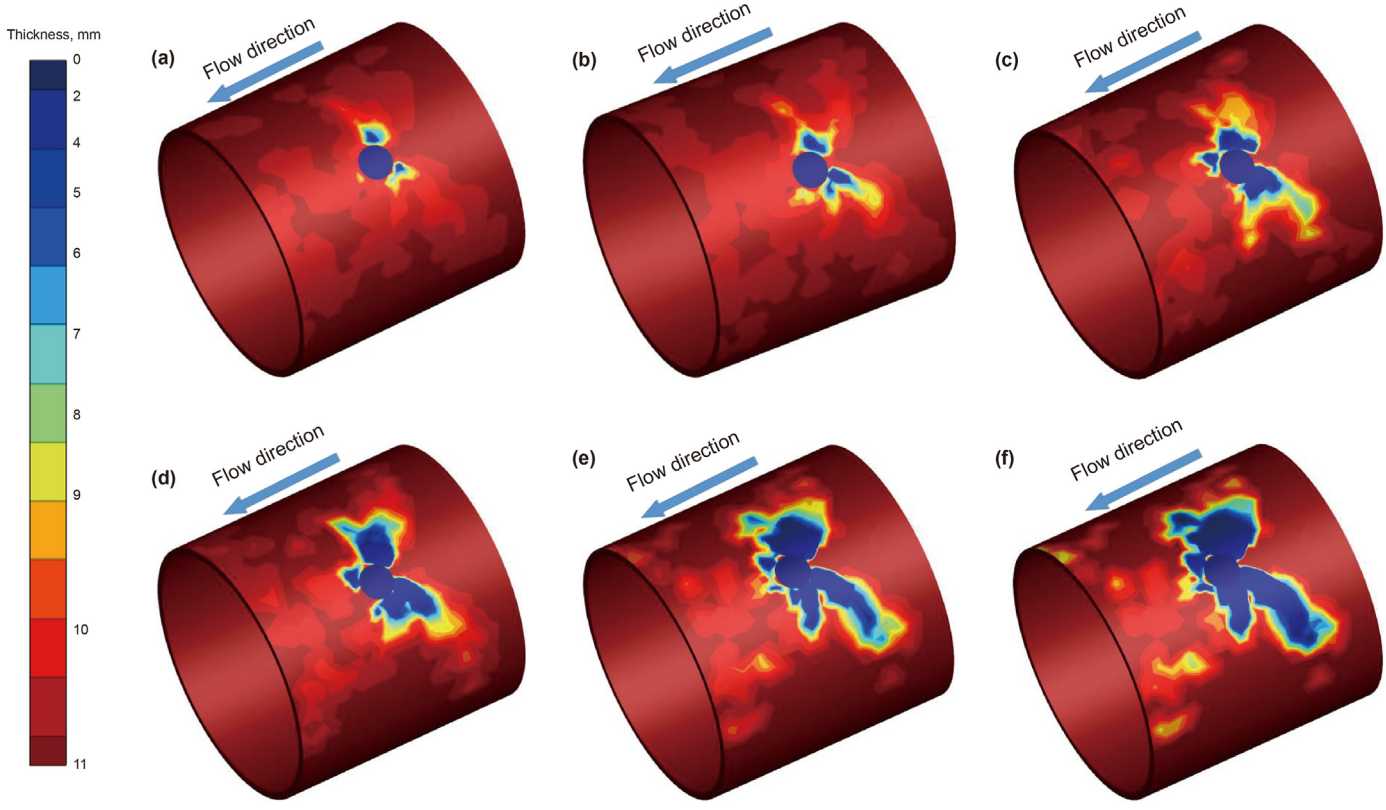

Fig. 8. Cloud diagrams of casing wall thickness near the perforation after erosion under different sand content: (**a**) 8%, (**b**) 11%, (**c**) 14%, (**d**) 17%, (**e**) 20%, and (**f**) 23%.

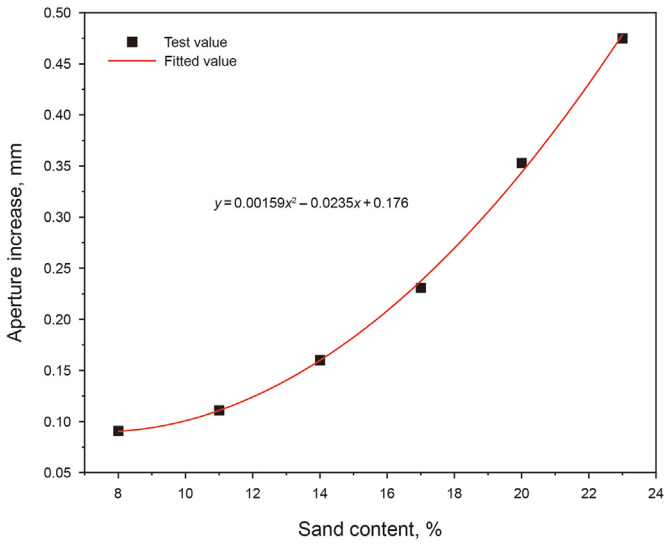

Fig. 9. Perforation diameter expansion after erosion under different sand content.

According to the data in Table 4 and Eq. (13), the elementary sequence and the subsequence of the original matrix and the dimensionless transformation from X to Y are determined, and the dimensionality of the matrix is normalized by means of meanization.

$$(X \to Y) = \begin{pmatrix} Y(1,1) & Y(1,2) & \cdots & Y(1,n) \\ Y(2,1) & Y(2,2) & \cdots & Y(2,n) \\ \vdots & \vdots & \ddots & \vdots \\ Y(m,1) & Y(m,2) & \cdots & Y(m,n) \end{pmatrix} \tag{12}$$

$$x'_{ij} = \frac{x_{ij}}{\overline{x_i}}, \quad \overline{x_i} = \frac{1}{m}\sum_{j=1}^{m} x_{ij} \tag{13}$$

The grey correlation coefficient is calculated to determine the correlation. The nature of the resolution coefficient is to control the influence of the maximum absolute difference on the overall correlation. Appropriate values are needed to qualitatively compare different influencing factors (Zuo et al., 2016; Jia et al., 2020). Generally, the range of the discrimination coefficient is 0–1. In this paper, the resolution coefficient is taken as 0.5 because there are few comparative factors.

$$\xi_i(k) = \frac{\min_{i=1}^{m} \min_{k=1}^{n} |x'_0(k) - x'_i(k)| + 0.5 \max_{i=1}^{m} \max_{k=1}^{n} |x'_0(k) - x'_i(k)|}{|x'_0(k) - x'_i(k)| + 0.5 \max_{i=1}^{m} \max_{k=1}^{n} |x'_0(k) - x'_i(k)|} \tag{14}$$

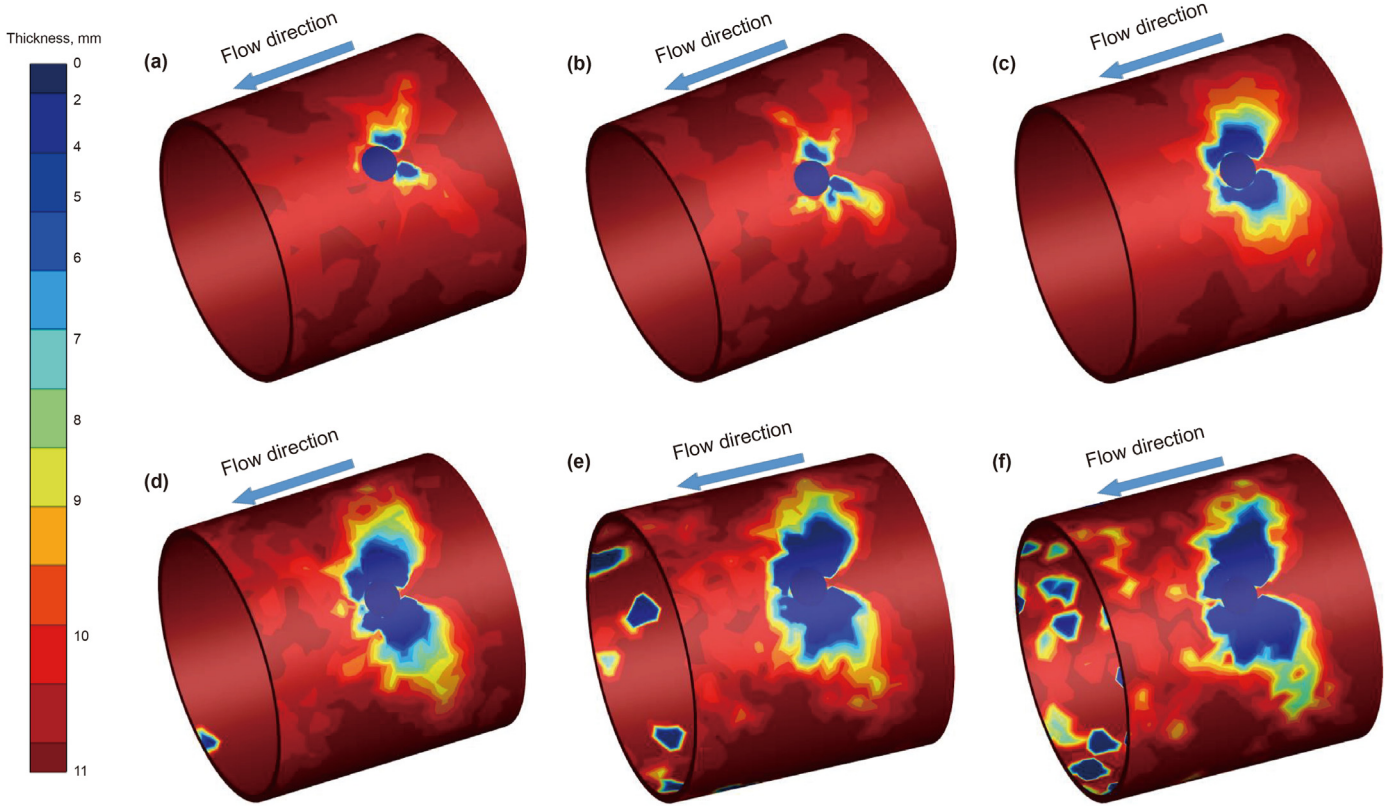

Fig. 10. Cloud diagrams of casing wall thickness near the perforation after erosion under different sand-passing quantities: (**a**) 1000 kg, (**b**) 2500 kg, (**c**) 4000 kg, (**d**) 5500 kg, (**e**) 7000 kg, and (**f**) 8500 kg.

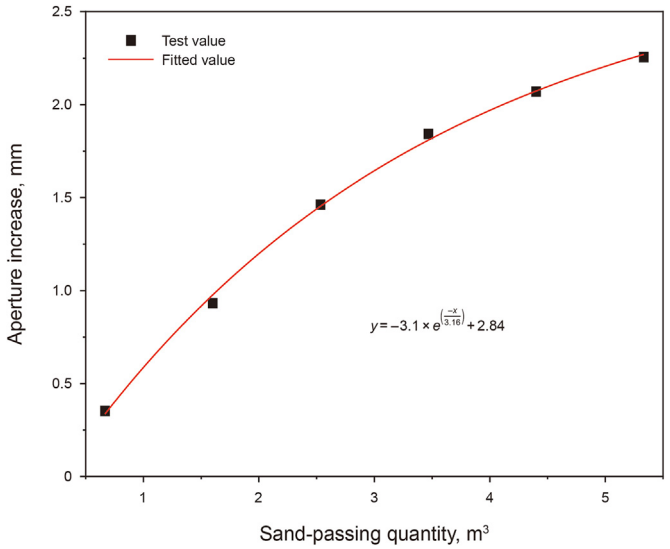

Fig. 11. Perforation diameter expansion after erosion under different sand-passing quantities.

$$r_i = \frac{1}{m}\sum_{j=1}^{m}\xi_{ij} \tag{15}$$

In the grey correlation analysis results (Table 5), among the three factors, the sand-passing quantity through the perforation had the most significant influence on perforation diameter expansion, followed by sand content, displacement had the least influence. In addition to this analysis method, the same results can also be obtained from the cloud diagrams of casing wall thickness near the perforation after erosion and fitting curve of perforation diameter expansion in Sections 3.1 to 3.3.

4. Establishment of perforation erosion prediction chart

4.1. Influence chart of displacement and sand content on diameter expansion

Based on the above research methods, when the sand-passing quantity was 0.67 m^3 and other fracturing parameters were fixed, the degree of erosion of perforation and surrounding casing wall under different fracturing displacements or different sand content of fracturing fluid was simulated. In the single perforation fracturing displacement range of 0.28–0.83 m^3/min and the sand content range of 8%~23%, with 36 sets of simulation data, the comprehensive influence surface diagram of perforation diameter expansion (Fig. 12) and the contour diagram of perforation diameter expansion (Fig. 13) are drawn.

Increasing the displacement and the sand content of the fracturing fluid will increase the perforation expansion. However, the spacing between contour lines is shrinking, which means that although the erosion rate is gradually increasing with the displacement and sand content, the growth rate of perforation expansion is gradually decreasing. Due to determined sand-passing quantity through the perforation, increasing the displacement or increasing the sand content will shorten the erosion time. So as the mass loss of the perforation increases per unit time, the growth rate of mass loss under this working condition will decrease.

When the displacement was 0.28 m^3/min and the sand content was 8%, the perforation diameter expansion was 0.023 mm, indicating that there was almost no perforation erosion. When the displacement increased to 0.83 m^3/min and the sand content increased to 23%, the perforation diameter expansion was 0.611 mm, suggesting the obvious perforation erosion.

4.2. Influence chart of sand content and sand-passing quantity on perforation diameter expansion

When the single perforation fracturing displacement was 0.61 m^3/min and other fracturing parameters were fixed, the influence of sand-passing quantity on perforation diameter expansion under different sand content of fracturing fluid was simulated. In the sand content range of 8%–23% and the sand-passing quantity of 0.67–5.67 m^3, with 36 sets of simulation data, the comprehensive influence surface diagram of perforation diameter expansion

Table 5
Judgment results of influence degree.

Parameter	Sand-passing quantity	Sand content	Displacement
Correlation coefficient	0.889	0.689	0.640
Rank	1	2	3

Table 4
Evaluation parameters and data of grey correlation analysis.

Sand-passing quantities, m^3	Displacement, m^3/min	Sand content, %	Perforation diameter increase, mm
0.67	0.28	11	0.094
0.67	0.39	11	0.104
0.67	0.5	11	0.123
0.67	0.61	11	0.16
0.67	0.72	11	0.221
0.67	0.83	11	0.317
0.67	0.61	8	0.091
0.67	0.61	11	0.111
0.67	0.61	14	0.16
0.67	0.61	17	0.231
0.67	0.61	20	0.353
0.67	0.61	23	0.475
0.67	0.61	20	0.353
1.67	0.61	20	0.933
2.67	0.61	20	1.463
3.67	0.61	20	1.843
4.67	0.61	20	2.071
5.67	0.61	20	2.256

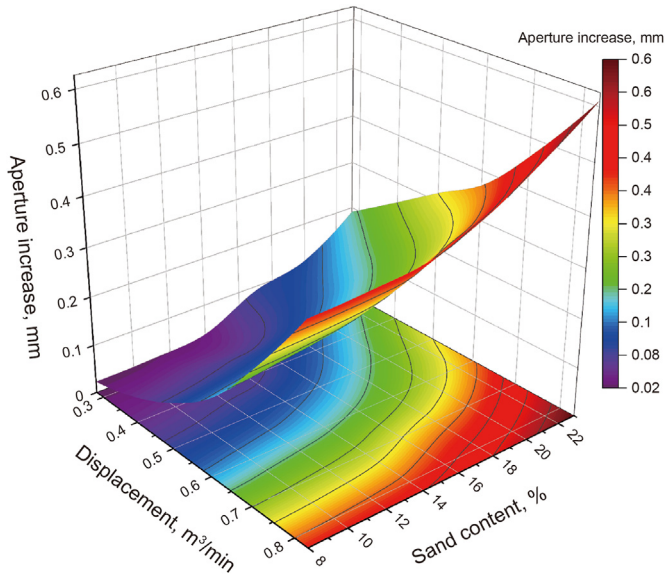

Fig. 12. Curved surface diagram of comprehensive influence of different displacement conditions and sand content on perforation erosion and diameter expansion.

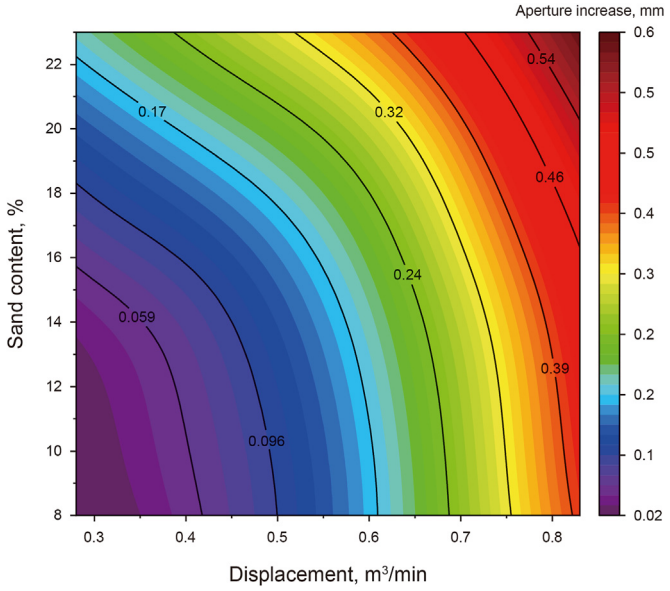

Fig. 13. Contour map of perforation erosion and diameter expansion under different displacements and sand content.

(Fig. 14) and the contour diagram of perforation diameter expansion (Fig. 15) are drawn.

Under a certain displacement, with the increase in the sand-passing quantity and the sand content of sand in the fracturing fluid, the perforation diameter expansion rate increased. The perforation diameter expansion rate increased with the increase in the sand content of sand and decreased with the increase in sand-passing quantity. Under different sand content, the influence surface diagram of sand-passing quantity on perforation diameter expansion showed special-shaped surfaces with different growth rates. When the sand-passing quantity was 0.67 m^3 and the sand content was 8%, the perforation diameter expansion was 0.091 mm, indicating that there was almost no perforation erosion. When the

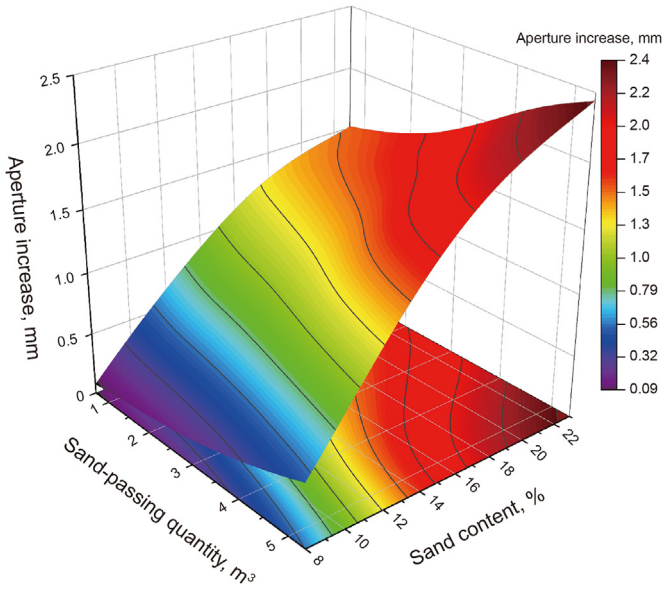

Fig. 14. Influence surface diagram of sand-passing quantity on perforation diameter expansion under different sand content.

sand-passing quantity was 5.67 m^3 and the sand content increased to 23%, the perforation diameter expansion was 2.414 mm, suggesting the obvious perforation erosion.

4.3. Influence chart of displacement and sand-passing quantity on diameter expansion

When the sand content of fracturing fluid was 20% and other fracturing parameters were fixed, the influence of sand-passing quantity on perforation diameter expansion under different single perforation fracturing displacements was simulated. With 36 sets of simulation data, in the displacement range of 0.28–0.83 m^3/min and the sand-passing quantity of 0.67–5.67 m^3, the comprehensive influence surface diagram of perforation diameter expansion (Fig. 16) and the contour diagram of perforation diameter expansion (Fig. 17) are drawn.

Under a certain sand content in the fracturing solution, with the increase in the sand-passing quantity and the displacement, the perforation diameter expansion increased. The perforation diameter expansion rate increased with the increase in displacement and decreased with the increase in sand-passing quantity. Under different displacements, the influence surface diagram of sand-passing quantity on perforation diameter expansion showed special-shaped surfaces with different growth rates. When the sand-passing quantity was 0.67 m^3 and the displacement was 0.28 m^3/min, the perforation diameter expansion was 0.273 mm, indicating that there was slight perforation erosion. When the sand-passing quantity was 5.67 m^3 and the displacement was 0.83 m^3/min, the perforation diameter expansion was 2.538 mm, suggesting the obvious perforation erosion.

5. Downhole perforation eagle detection and erosion degree verification

5.1. Testing tools

Optis infinity 360-degree circular scanning GB-pixel technology was adopted in the study (Fig. 18). The sensor part of the system

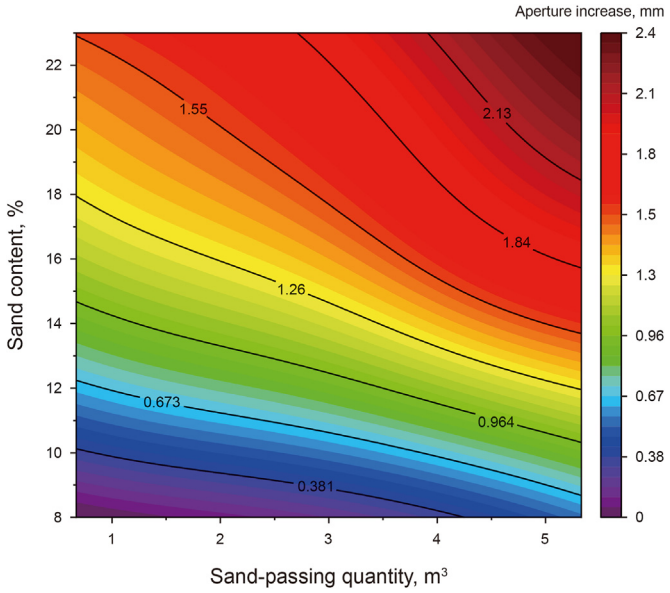

Fig. 15. Contour map of sand-passing quantity and perforation diameter expansion under different sand content.

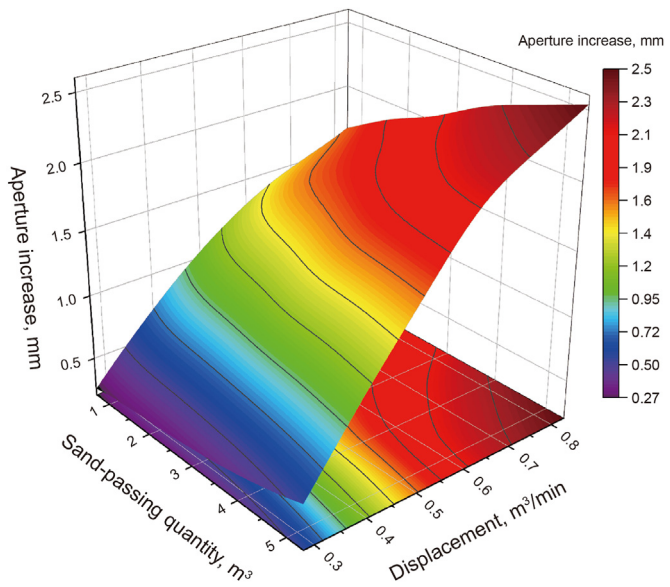

Fig. 16. Influence surface diagram of sand-passing quantity on perforation diameter expansion under different displacement conditions.

consists of four dual-variable LED lighting arrays at the top and bottom and can simultaneously capture four video streams in the 360-degree full coverage of the wellbore. Roberts et al. (2018) described the system in detail. The system memory and image acquisition use a coiled tubing, the image capture efficiency of the system is also improved because the 360-degree coverage of casing wall means that all perforations pass through the lens regardless of camera position, the pixel processing capacity can reaches 4 m/min.

5.2. Overview of test wells

There are three test wells in the same development layer, which are divided into well A, well B and well C. Well B and well C are

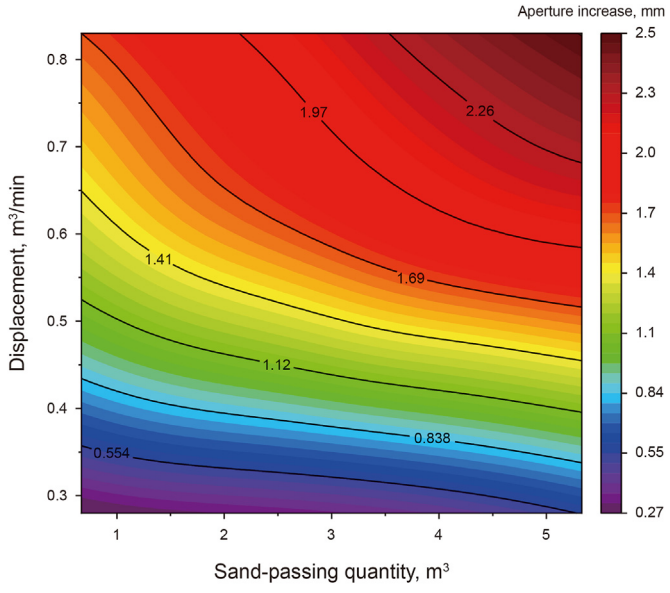

Fig. 17. Contour map of sand-passing quantity and perforation diameter expansion under different displacement conditions.

perforation erosion control research wells. The research and working condition setting in this paper are based on the second stage of the second development part of test well A. This development stage is located in the eighth stage of the whole well. There are 6 clusters of perforations in this construction stage, with 3 perforation in each cluster. The temporary plugging process is adopted during the fracturing construction. The displacement, sand addition and proppant particle size are consistent in post-temporary and pre-temporary.

The horizontal section of the well A was 946 m long and divided into two parts. The first construction and reconstruction part involved 6 stages/32 clusters in the depth range of 4587~5159 m. The length of the reconstruction stage was 483.2 m long. The test part included 2–6 stages with 6 clusters in each stage. The cluster spacing was 5.5–24 m/13.8 m and the length of a single stage was about 80 m. The second part involved 4 stages/24 clusters in the depth range of 4302~4541 m. The reconstruction stage was 215.1 m long and each stage contained 6 clusters (Fig. 19).

5.3. Downhole erosion test results

With the Optis Infinity Eagle logging technology, the well B and well C were collected images after the fracturing operation, and the well A were collected images in post-temporary and pre-temporary. Due to the bridge plug displacement and other downhole complex conditions, the actual number of plugged perforations and the statistics of sand and liquid inflow in each construction stage will have deviation. Therefore, some stages with double bridge plugs and no bridge plug displacement are selected as research and reference.

In this paper, the main research object is stage 8 of well A, and the perforation erosion reference objects are stage 17 of well B and stage 7 of well C. In the pre-temporary plugging stage, a total of 90 m^3 sand in stage 8 of well A was added and fracturing construction displacement was 10 m^3/min (single perforation 0.56 m^3/min). The particle size of proppant was 40/70 mesh. Eagle logging was carried out after fracturing construction. Well A stage 8 had 6 clusters (18 perforations) in total. In the first eagle logging, 17

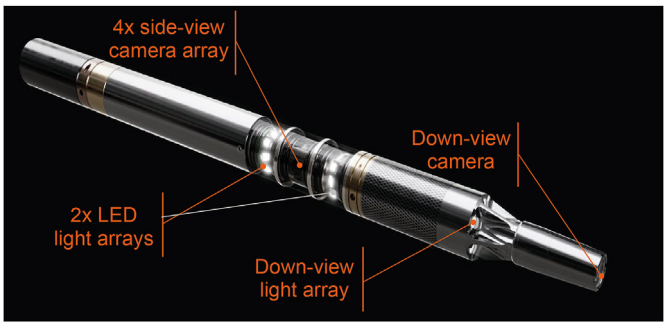

Fig. 18. Configuration of the latest array side-view video sensor of Optis infinity technology.

perforations were found and the first perforation in the first cluster was suspected to be buried by sand. The buried perforation was found to be not eroded in the second eagle logging because it had good roundness. The image and information of a specific perforation could be obtained by intercepting and analyzing the eagle logging video. As shown in Fig. 20, except the first perforation in the first cluster, in the remaining 17 perforations, the maximum erosion area was 198.9 mm^2 and the minimum erosion area was 2.3 mm^2. The seriously eroded perforations were special-shaped perforations.

According to the downhole eagle detection data, the perforation conditions in well A stage 8 in the pre-temporary plugging stage are shown in Table 6.

90 m^3 of 40/70 mesh quartz sand is added to well A stage 8 in pre-temporary plugging stage. The average perforation erosion area is 73.2 mm^2, and the standard deviation is 65.7. All perforations had sand and liquid flows in the pre-temporary plugging stage, as indicated in the perforation erosion data. Assuming that sand and liquid flows into each perforation were uniform, the sand-passing quantity of each perforation was 5 m^3. In stage 8 of well A, the fluid intensity in sand fracturing was 10.6 m^3/m and the proppant concentration was 2.2 m^3/m. The sand content in the fracturing fluid was about 21%. The comparison results of the field eagle data and the established charts of perforation sand-passing quantity and perforation diameter expansion amount under different displacement conditions are shown in Fig. 21. In pre-temporary plugging stage, the average erosion area of all perforations was 73.2 mm^2, and the average diameter expansion value of perforations was 2.05 mm. According to the numerical simulation calculation charts, the diameter expansion value was 2.15 mm and the error was 4.6%.

The same method was used to analyze stage 17 of well B and stage 7 of well C. There are 6 clusters in stage 17 of well B and 3 perforations in a single cluster without temporary plugging. A total of 75 m^3 of 40/70 mesh quartz sand is added. The average sand-passing quantity of the perforation is 4.1 m^3, the fluid intensity in sand fracturing was 5.88 m^3/m and the proppant concentration was 1.0 m^3/m. The sand content in the fracturing fluid was about 17%. The average displacement of the single stage is 11 m^3/min (the displacement of the single perforation is 0.61 m^3/min). The comparison results of the field eagle data and the established charts of perforation sand-passing quantity and perforation diameter expansion amount under different sand content conditions are shown in Fig. 22. The average diameter expansion value of perforations was 1.8 mm. According to the numerical simulation calculation charts, the diameter expansion value was 1.7 mm and the error was 5.4%.

Section 7 of well C had 6 clusters and 8 perforations in a single cluster, without temporary plugging. A total of 32 m^3 of 40/70 mesh quartz sand is added. The average sand-passing quantity of the perforation is 0.67 m^3, the fluid intensity in sand fracturing was 4.35 m^3/m and the proppant concentration was 0.87 m^3/m. The sand content was about 20%. The average displacement of the single stage is 11 m^3/min (the displacement of the single perforation is 0.61 m^3/min). The comparison results of the field eagle data and the established charts are shown in Fig. 23. The average diameter expansion value of perforations was 0.33 mm. The value of numerical simulation calculation charts was 0.35 mm and the error was 6%, indicating the established charts were the valuable reference.

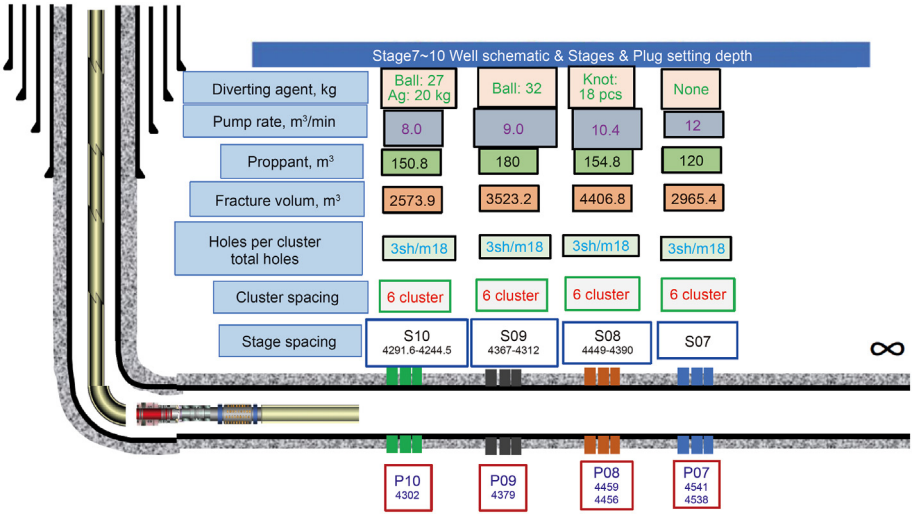

Fig. 19. Well A design drawing of the second development part of reconstruction.

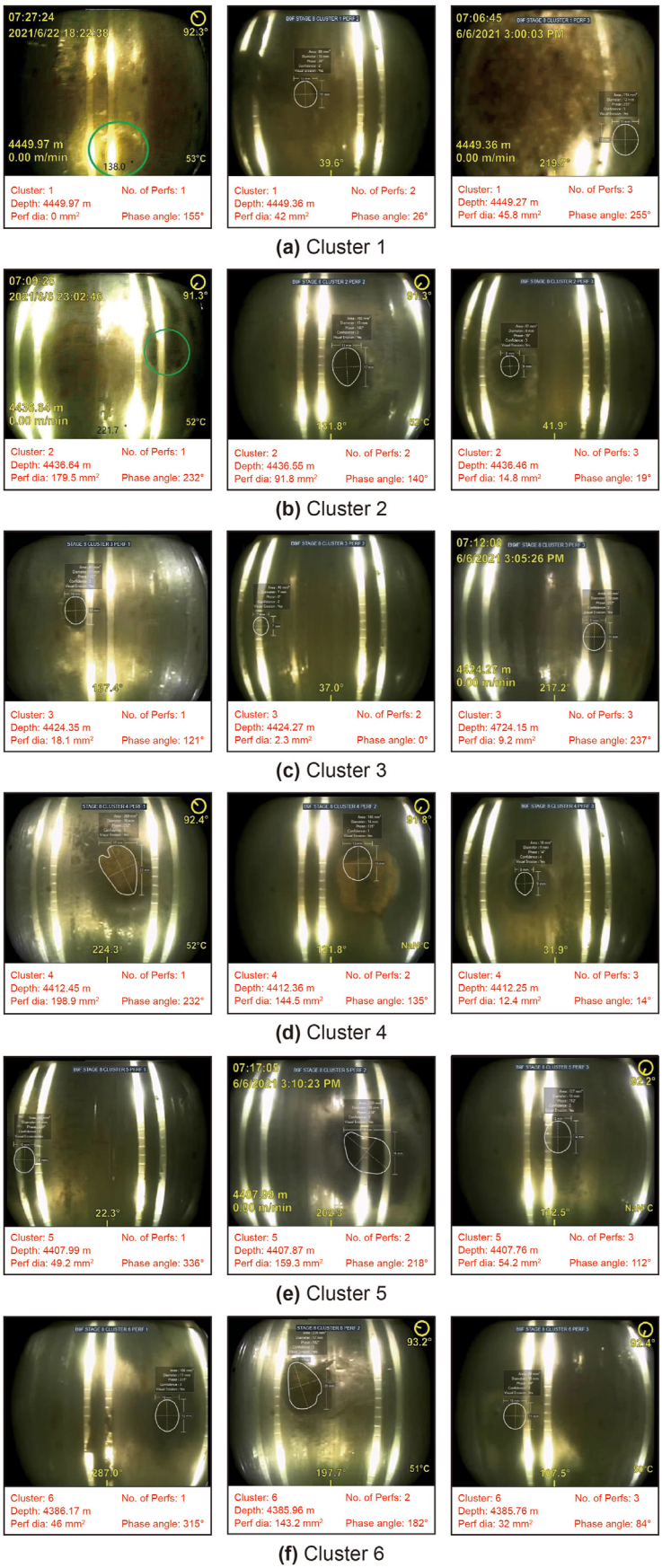

Fig. 20. Eagle logging images of well A stage 8 for the first time (in the pre-temporary plugging stage).

Table 6
Statistics of perforation information in Stage 8 in the pre-temporary plugging stage.

Quantity of clusters	Phase angle, °	Depth, m	Erosion area, mm^2
Perf. 1 of Cluster 1	155	4449.97	0
Perf. 2 of Cluster 1	26	4449.36	42
Perf. 3 of Cluster 1	255	4449.27	45.8
Perf. 1 of Cluster 2	232	4436.64	179.5
Perf. 2 of Cluster 2	140	4436.55	91.8
Perf. 3 of Cluster 2	19	4436.46	14.8
Perf. 1 of Cluster 3	121	4424.35	18.1
Perf. 2 of Cluster 3	0	4424.27	2.3
Perf. 3 of Cluster 3	237	4424.15	9.2
Perf. 1 of Cluster 4	232	4412.45	198.9
Perf. 2 of Cluster 4	135	4412.36	144.5
Perf. 3 of Cluster 4	14	4412.25	12.4
Perf. 1 of Cluster 5	336	4407.99	49.2
Perf. 2 of Cluster 5	218	4407.87	159.3
Perf. 3 of Cluster 5	112	4407.76	54.2
Perf. 1 of Cluster 6	315	4386.17	46
Perf. 2 of Cluster 6	182	4385.96	143.2
Perf. 3 of Cluster 6	84	4385.76	84

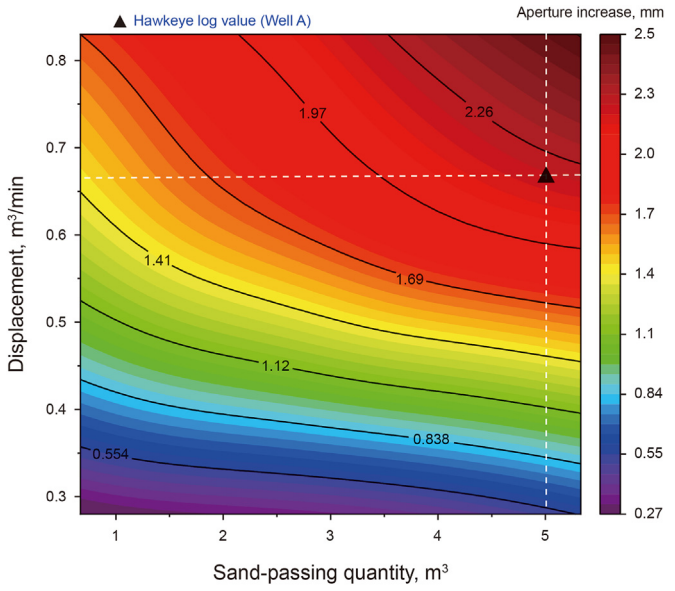

Fig. 21. Comparison between the contour diagram of comprehensive influence of different displacements and perforation sand-passing quantity with logging data of well A stage 8.

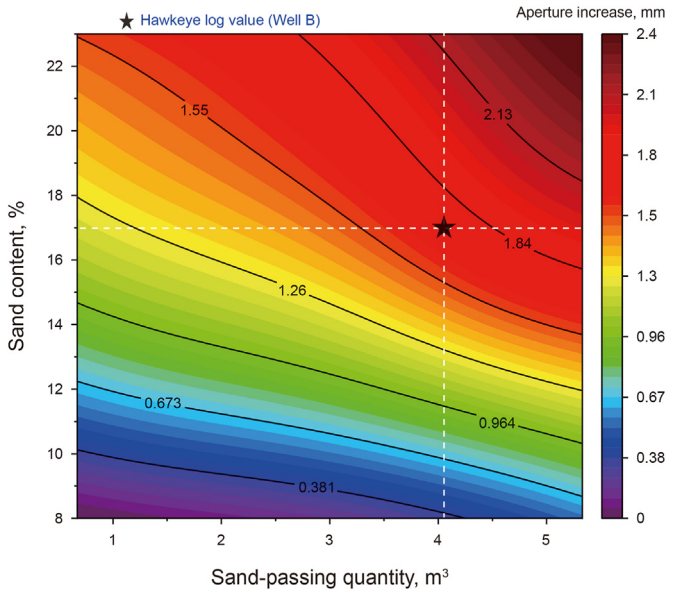

Fig. 22. Comparison between the contour diagram of comprehensive influence of different sand content and perforation sand-passing quantity with logging data of well B stage 17.

6. Conclusions

Firstly, the calculation models of casing perforation wall thickness loss and perforation diameter expansion during sand fracturing were established. The influences of various fracturing construction parameters on perforation diameter expansion were decreased according to the following order: perforation sand-passing quantity > sand content > displacement.

Secondly, the influence relationship between fracturing parameters and perforation erosion expansion was obtained: diameter expansion increased gradually with the increase in displacement, sand content, and perforation sand-passing quantity. When the sand-passing quantity increased from 0.67 to 5.67 m^3, the perforation diameter expansion increased from 0.33 to 2.23 mm. With the increase in displacement and sand content, the diameter expansion rate increased significantly. With the increase in the sand-passing quantity, the diameter expansion rate decreased gradually and tended to a critical value. Therefore, low displacement or low sand content was suggested in the initial stage of fracturing operation and then displacement or low sand content could be increased gradually.

Thirdly, through the simulation calculation with 108 sets of data, the influence charts of various fracturing parameters on casing perforation expansion were respectively established. The perforation erosion images after fracturing construction were obtained with the downhole eagle logging technology to verify the

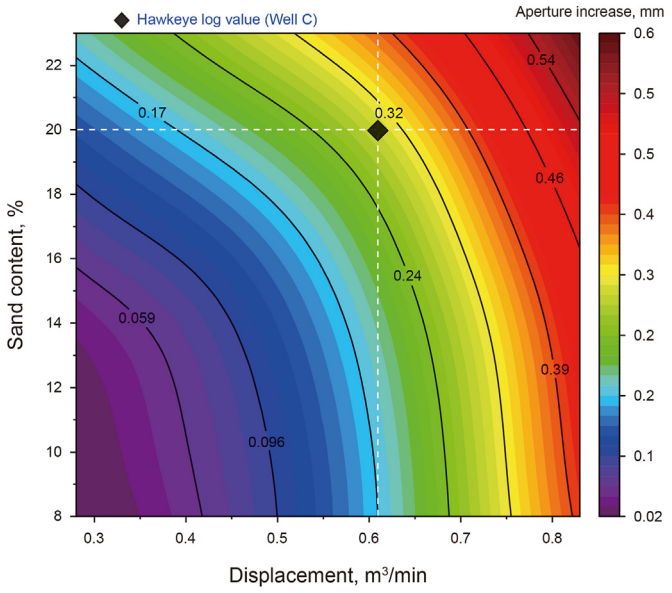

Fig. 23. Comparison between the contour diagram of comprehensive influence of different sand content and displacement with logging data of well C stage 7.

established charts. The error between the predicted value of the charts and the actual perforation erosion result was about 5%, suggesting the reliability and guidance value of the charts.

Declaration of competing interest

The authors declare that they are no known competing financial interests or personal relationships that could have appeared to influence the work reported in this paper.

Acknowledgements

The authors acknowledge the support from Sichuan Science and Technology Program (21JCQN0066) and supported by National Natural Science Foundation of China (No. 51774249).

References

Al-Fatlawi, O., Hossain, M., Patel, N., et al., 2019. Evaluation of the Potentials for Adapting the Multistage Hydraulic Fracturing Technology in Tight Carbonate Reservoir. In: SPE Middle East Oil and Gas Show and Conference.
ANSYS FLUENT Theory Guide, 2020. FLUENT Inc.
Bakhshi, E., Golsanami, N., Chen, L., 2021. Numerical modeling and lattice method for characterizing hydraulic fracture propagation: a review of the numerical, experimental, and field studies. Arch. Comput. Methods Eng. 28 (5), 3329–3360. https://doi:10.1007/s11831-020-09501-6.
Bitter, J., 1963. A study of erosion phenomena: Part II. Wear 6 (3), 169–190. https://doi:10.1016/0043-1648(63)90073-5.
Chen, S., Zhang, Q., Mclellan, B., et al., 2020. Review on the petroleum market in China: history, challenges and prospects. Petrol. Sci. 17 (6), 1779–1794. https://doi:10.1007/s12182-020-00501-6.
Costa, P., Picano, F., Brandt, L., et al., 2018. Effects of the finite particle size in turbulent wall-bounded flows of dense suspensions. J. Fluid Mech. 843 (1), 450–478. https://doi:10.1017/jfm.2018.117.
Crump, J., Conway, M., 1988. Effects of perforation-entry friction on bottomhole treating analysis. J. Petrol. Technol. 40 (8), 1041–1048. https://doi:10.2118/15474-PA.
Evans, A., 1978. Impact damage in brittle materials in the elastic-plastic response regime. J. Appl. Phys. 49 (6), 3304–3310. https://doi:10.1098/rspa.1978.0106.
Finnie, I., 1958. The Mechanism of Erosion of Ductile Metals. In: 3rd US National Congress of Applied Mechanics, New York, pp. 527–532.
Finnie, I., McFadden, D., 1978. On the velocity dependence of the erosion of ductile metals by solid particles at low angles of incidence. Wear 48 (1), 181–190. https://doi:10.1016/0043-1648(78)90147-3.
Fleming, J., Suh, N., 1977. Mechanics of crack propagation in delamination wear. Wear 44, 39–56. https://doi:10.1016/0043-1648(77)90083-7.
Hossain, M.M., Al-Fatlawi, O., Brown, D., et al., 2018. Numerical Approach for the Prediction of Formation and Hydraulic Fracture Properties Considering Elliptical Flow Regime in Tight Gas Reservoirs. OTC, Kuala Lumpur, Malaysia. https://doi:10.4043/28418-MS.
Hutchings, I., 1981. A model for the erosion of metals by spherical-particles at normal incidence. Wear 70 (3), 269–281. https://doi:10.1016/0043-1648(81)90347-1.
Jia, E., Zeng, Y., Jin, Y., et al., 2020. Heat dissipation investigation of the power lithium-ion battery module based on orthogonal experiment design and fuzzy grey relation analysis. Energy 211, 118596. https://doi:10.1016/j.energy.2020.118596.
Jignesh, T., Jyotirmay, B., 2016. Influence of intermittent flow sub-patterns on erosion-corrosion in horizontal pipe. J. Petrol. Sci. Eng. 145, 298–320. https://doi:10.1016/j.petrol.2016.05.006.
Launder, B., Spalding, D., 1974. The numerical computation of turbulent flows. Comput. Methods Appl. Mech. Eng. 3 (2), 269–289. https://doi:10.1016/0045-7825(74)90029-2.
Levy, A., 1983. The effects of erodent composition and shape on the erosion of steel. Wear 89 (2), 151–162. https://doi:10.1016/0043-1648(83)90240-5.
Long, G., Liu, S., Xu, G., et al., 2018. A perforation-erosion model for hydraulic-fracturing applications. SPE Prod. Oper. 33 (4), 770–783. https://doi:10.2118/174959-PA.
Long, G., Xu, G., 2017. The effects of perforation erosion on practical hydraulic-fracturing. SPE J. 22 (2), 645–659. https://doi:10.2118/185173-PA.
Melikoglu, M., 2014. Shale gas: analysis of its role in the global energy market. Renew. Sustain. Energy Rev. 37, 460–468. https://doi:10.1016/j.rser.2014.05.002.
Mohammed, A., Oyeneyin, B., Bartlett, M., et al., 2020. Prediction of casing critical buckling during shale gas hydraulic fracturing. J. Petrol. Sci. Eng. 185, 106655. https://doi:10.1016/j.petrol.2019.106655.
Parsi, M., Agrawal, M., Srinivasan, V., et al., 2015a. CFD simulation of sand particle erosion in gas-dominant multiphase flow. J. Nat. Gas Sci. Eng. 27, 706–718. https://doi:10.1016/j.jngse.2015.09.003.
Parsi, M., Vieira, R., Kesana, N., et al., 2015b. Ultrasonic measurements of sand particle erosion in gas dominant multiphase churn flow in vertical pipes. Wear 328–329, 401–413. https://doi:10.1016/j.wear.2015.03.013.
Pereira, G., Souza, F., Moro Marting, D., 2014. Numerical prediction of the erosion due to particles in elbows. Powder Technol. 261, 105–117. https://doi:10.1016/j.powtec.2014.04.033.
Roberts, G., Jeff, W., Joe, M., et al., 2020. Proppant Distribution Observations from 20000+ Perforation Erosion Measurements. In: SPE–199693–MS, Hydraulic Fracturing Technology Conference and Exhibition. Woodlands, Texas, USA. https://doi:10.2118/199693-MS.
Roberts, G., Lilly, T., Tymons, E., 2018. Improved Well Stimulation Through the Application of Downhole Video Analytics. In: SPE–189851–MS, Hydraulic Fracturing Technology Conference and Exhibition. Woodlands, Texas, USA. https://doi:10.2118/189851-MS.
Shi, B., Chang, X., Yin, W., et al., 2019. Quantitative evaluation model for tight sandstone reservoirs based on statistical methods - a case study of the Triassic Chang 8 tight sandstones, Zhenjing area, Ordos Basin, China. J. Petrol. Sci. Eng. 173, 601–616. https://doi:10.1016/j.petrol.2018.10.035.
Suzuki, M., Inaba, K., Yammoto, M., 2008. Numerical simulation of sand erosion in a square-section 90-degree bend. J. Fluid Sci. Technol. 3 (7), 868–880. https://doi:10.1299/kikaib.74.1478.
Tilly, G., 1973. A two stage mechanism of ductile erosion. Wear 23, 87–96. https://doi:10.1016/0043-1648(73)90044-6.
Tilly, G., 1979. Erosion caused by impact of solid particles. Treatise on Mater. Sci. Technol. 13, 287–319. https://doi:10.1016/S0161-9160(13)70071-1.
Wang, J., 2020. Continuum theory for dense gas-solid flow: a state-of-the-art review. Chem. Eng. Sci. 215, 115428. https://doi:10.1016/j.ces.2019.115428.
Wu, B., Zhang, S., Li, J., et al., 2022. Simulation of the erosion of casing and perforation under staged sand fracturing conditions in horizontal sections. J. Hydrodyn. 34 (4), 725–743. https://doi:10.1007/s42241-022-0050-3.
Xu, J., Mou, Y., Xue, C., et al., 2021. The study on erosion of buckling tubing string in HTHP ultra-deep wells considering fluid - solid coupling. Energy Rep. 7, 3011–3022. https://doi:10.1016/j.egyr.2021.05.035.
Yang, S., Zhang, L., Fan, J., et al., 2021. Experimental study on erosion behavior of fracturing pipeline involving tensile stress and erosion prediction using random forest regression. J. Nat. Gas Sci. Eng. 87 (1–4), 103760. https://doi:10.1016/j.jngse.2020.103760.
Zeng, D., Zhang, E., Ding, Y., et al., 2018. Investigation of erosion behaviors of sulfur-particle-laden gas flow in an elbow via a CFD-DEM coupling method. Powder Technol. 329, 115–128. https://doi:10.1016/j.powtec.2018.01.056.
Zeng, H., Jin, Y., Qu, H., et al., 2022. Experimental investigation and correlations for proppant distribution in narrow fractures of deep shale gas reservoirs. Petrol. Sci. 19 (2), 619–628. https://doi:10.1016/j.petsci.2021.10.019.
Zhang, J., Kang, J., Fan, J., et al., 2016. Research on erosion wear of high-pressure pipes during hydraulic fracturing slurry flow. J. Loss Prev. Process. Ind. 43 (1), 438–448. https://doi:10.1016/j.jlp.2016.07.008.

Zhang, Y., 2006. Application and Improvement of Computational Fluid Dynamics (CFD) in Solid Particle Erosion Modeling. Doctoral dissertation,. The University of Tulsa, Tulsa, Oklahoma, USA.

Zhang, Y., Reuterfors, E., Mclaury, B., et al., 2007. Comparison of computed and measured particle velocities and erosion in water and air flows. Wear 263 (1), 330–338. https://doi:10.1016/j.wear.2006.12.048.

Zhao, Y., Tang, C., Yao, J., et al., 2020. Investigation of erosion behavior of 304 stainless steel under solid-liquid jet flow impinging at 30. Petrol. Sci. 17 (4), 1135–1150. https://doi:10.1007/s12182-020-00473-7.

Zheng, Y., Wang, H., Li, Y., et al., 2022. Effect of proppant pumping schedule on the proppant placement for supercritical CO2 fracturing. Petrol. Sci. 19 (2), 628–638. https://doi:10.1016/j.petsci.2021.11.002.

Zhu, H., Lin, Y., Zeng, D., et al., 2012. Numerical analysis of flow erosion on drill pipe in gas drilling. Eng. Fail. Anal. 22, 83–91. https://doi:10.1016/j.engfailanal.2012.01.007.

Zhu, R., Zhou, P., Zhou, C., et al., 2019. Fuzzy grey relational analysis for influencing factors of heat transfer in a blast furnace hearth. Ironmak. Steelmak. 45 (10), 899–906. https://doi:10.1080/03019233.2017.1410967.

Zuo, W., Liu, X., Peng, Q., et al., 2016. Orthogonal experimental design and fuzzy grey relational analysis for emitter efficiency of the micro-cylindrical combustor with a step. Appl. Therm. Eng. 103, 945–951. https://doi:10.1016/j.applthermaleng.2016.04.148.